TESS's first planet: A super-Earth transiting the naked-eye star π Mensae

A&A 619, L10 (2018)
https://doi.org/10.1051/0004-6361/201834289

Astronomy & Astrophysics

LETTER TO THE EDITOR

TESS's first planet

A super-Earth transiting the naked-eye star π Mensae*

D. Gandolfi[1], O. Barragán[1], J. H. Livingston[2], M. Fridlund[3,4], A. B. Justesen[5], S. Redfield[6], L. Fossati[7], S. Mathur[8,9], S. Grziwa[10], J. Cabrera[11], R. A. García[12,13], C. M. Persson[3], V. Van Eylen[14], A. P. Hatzes[15], D. Hidalgo[8,9], S. Albrecht[5], L. Bugnet[12,13], W. D. Cochran[16], Sz. Csizmadia[11], H. Deeg[8,9], Ph. Eigmüller[11], M. Endl[16], A. Erikson[11], M. Esposito[15], E. Guenther[15], J. Korth[10], R. Luque[8,9], P. Montañes Rodríguez[8,9], D. Nespral[8,9], G. Nowak[8,9], M. Pätzold[10], and J. Prieto-Arranz[8,9]

(Affiliations can be found after the references)

Received 20 September 2018 / Accepted 28 September 2018

ABSTRACT

We report on the confirmation and mass determination of π Men c, the first transiting planet discovered by NASA's TESS space mission. π Men is a naked-eye (V = 5.65 mag), quiet G0 V star that was previously known to host a sub-stellar companion (π Men b) on a long-period (P_{orb} = 2091 days), eccentric (e = 0.64) orbit. Using TESS time-series photometry, combined with *Gaia* data, published UCLES at AAT Doppler measurements, and archival HARPS at ESO-3.6m radial velocities, we found that π Men c is a close-in planet with an orbital period of P_{orb} = 6.27 days, a mass of M_c = 4.52 ± 0.81 $M_\oplus$, and a radius of R_c = 2.06 ± 0.03 $R_\oplus$. Based on the planet's orbital period and size, π Men c is a super-Earth located at, or close to, the radius gap, while its mass and bulk density suggest it may have held on to a significant atmosphere. Because of the brightness of the host star, this system is highly suitable for a wide range of further studies to characterize the planetary atmosphere and dynamical properties. We also performed an asteroseismic analysis of the TESS data and detected a hint of power excess consistent with the seismic values expected for this star, although this result depends on the photometric aperture used to extract the light curve. This marginal detection is expected from pre-launch simulations hinting at the asteroseismic potential of the TESS mission for longer, multi-sector observations and/or for more evolved bright stars.

Key words. planetary systems – planets and satellites: detection – planets and satellites: fundamental parameters – planets and satellites: terrestrial planets – stars: fundamental parameters

1. Introduction

Successfully launched on 18 April 2018, NASA's Transiting Exoplanet Survey Satellite (TESS; Ricker et al. 2015) will provide us with a leap forward in understanding the diversity of small planets ($R_p < 4\,R_\oplus$). Unlike previous space missions, TESS is performing an all-sky transit survey focusing on bright stars ($5 < V < 11$ mag) so that detailed characterizations of the planets and their atmospheres can be performed. In its two-year prime mission, TESS observes first the southern and then the northern ecliptic hemisphere. The survey is broken up into 26 anti-solar sky sectors. TESS uses four cameras to observe each sector, resulting in a combined field of view of 24° × 96°. The overlap between sectors towards the ecliptic poles provides greater sensitivity to smaller and longer-period planets in those regions of the celestial sphere. TESS records full-frame images of its entire field of view every 30 min and observes approximately 200 000 pre-selected main-sequence stars with a cadence of ∼2 min. The mission will certainly open a new era in the study of close-in small planets, providing us with cornerstone objects amenable to both mass determination – via Doppler spectroscopy – and atmospheric characterization – via transmission spectroscopy with NASA's *James Webb* Space Telescope (JWST) and the next generation of extremely large ground-based telescopes (ELT, TMT, and GMT).

Following a successful commissioning of 3 months, TESS started the science operation on 25 July 2018 by photometrically monitoring its first sector (Sector 1), which is centered at coordinates $\alpha = 352.68°$, $\delta = -64.85°$ (J2000). Shortly after ∼30 days of (almost) continuous observations in Sector 1, 73 transiting planet candidates were detected in the two-minute cadence light curves by the TESS team and made available to the scientific community upon registration to a dedicated web portal hosted at the Massachusetts Institute of Technology (MIT) web page[1].

In this letter, we present the spectroscopic confirmation of π Men c, the first transiting planet discovered by the TESS space mission. The host star is π Mensae (HD 39091; Table 1), a naked-eye (V = 5.65 mag), relatively inactive ($\log R'_{HK} = -4.941$; Gray et al. 2006) G0 V star already known to host a sub-stellar companion (π Men b) on a ∼2100-day eccentric ($e \approx 0.6$) orbit (Jones et al. 2002). π Men c is a 2.06 $R_\oplus$ planet with an orbital period of 6.27 days. Using *Gaia* photometry, archival HARPS Doppler data, and published UCLES high-precision radial velocities (RVs) we confirmed the planetary nature of the transiting signal detected by TESS and derived the planet's mass. We note

* The entire RV data (Tables A.1, A.3 and full Table A.2) are only available at the CDS via anonymous ftp to cdsarc.u-strasbg.fr (130.79.128.5) or via http://cdsarc.u-strasbg.fr/viz-bin/qcat?J/A+A/619/L10

[1] Available at https://tess.mit.edu/alerts/

Table 1. Main identifiers, coordinates, and parallax, optical, and infrared magnitudes of π Men.

Parameter	Value	Source
HD	39091	
TIC ID	261136679	TIC
TOI ID	144	TESS Alerts
Gaia DR2 ID	4623036865373793408	*Gaia* DR2
RA (J2000)	05 37 09.885	*Gaia* DR2
RA (J2000)	−80 28 08.831	*Gaia* DR2
π	54.705 ± 0.0671 mas	*Gaia* DR2
V	5.65 ± 0.01	Mermilliod (1987)
B	6.25 ± 0.01	Mermilliod (1987)
J	4.869 ± 0.272	2MASS
H	4.424 ± 0.226	2MASS
K_s	4.241 ± 0.027	2MASS
G	5.4907 ± 0.0014	*Gaia* DR2
G_{BP}	5.8385 ± 0.0041	*Gaia* DR2
G_{RP}	5.0643 ± 0.0034	*Gaia* DR2

Notes. Values marked with TIC, *Gaia* DR2, and 2MASS are from Stassun et al. (2018), Gaia Collaboration (2018), and Cutri et al. (2003), respectively.

that in the final stage of preparing this manuscript, an independent investigation of this system was publicly announced by Huang et al. (2018).

2. TESS photometry

We downloaded the TESS Sector 1 light curves from the MIT web site. For the TESS object of interest TOI-144 (π Men, HD 39091, TIC 261136679), the light curve is provided by the NASA Ames Science Processing Operations Center (SPOC). The time-series includes 18 036 short-cadence ($T_{exp} = 2$ min) photometric measurements. TESS observations started on 25 July 2018 and ended on 22 August 2018. We removed any measurements that have a non-zero "quality" flag, that is, those suffering from cosmic rays or instrumental issues. We removed any long-term stellar variability by fitting a cubic spline with a width of 0.75 days. We searched the light curve for transit signals using the Box-least-squares algorithm (BLS; Kovács et al. 2002). We detected the signal of π Men c with a signal-to-noise ratio (S/N) of 9.1 and our ephemeris is consistent with that reported by the TESS team. We did not find any additional transit signal with $S/N > 6$. We also performed a periodogram and auto-cross-correlation analysis in an attempt to extract the rotation period of the star from the out-of-transit TESS light curve, but we found no significant rotation signal in the light curve.

3. Limits on photometric contamination

As a result of the ~21″ pixel scale of the TESS detectors, photometric contamination due to chance alignment with a background source is more likely than in previous transit surveys, such as *Kepler*. We investigated this possibility using archival images of π Men from the SERC-J and AAO-SES surveys[2] and *Gaia* DR2 (Gaia Collaboration 2018). The TESS photometric aperture used to create the SPOC light curve is approximately 6 × 6 TESS pixels in extent. We thus executed a query of *Gaia* DR2 centered on the coordinates of π Men from the TESS Input Catalog[3] (TIC; Stassun et al. 2018) using a search radius of 2′. The archival images were taken in 1978 and 1989, and therefore π Men appears significantly offset from its current position due to proper motion; no background source is visible near the current position of π Men. Figure 1 shows *Gaia* DR2 source positions overplotted on the archival images, along with the SPOC photometric aperture.

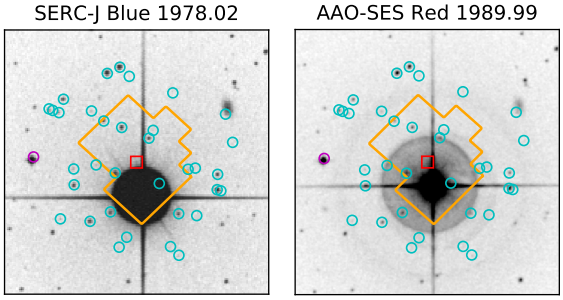

Fig. 1. 5′×5′ archival images with the SPOC photometric aperture overplotted in orange, the *Gaia* DR2 position (J2015.5) of π Men indicated by a red square, and other *Gaia* DR2 sources within 2′ of π Men indicated by circles. The magenta circle indicates the position of *Gaia* DR2 4623036143819289344, a nearby source bright enough to be the host of the observed transit signals (see Sect. 3), and cyan circles indicate sources that are too faint.

Assuming a maximum eclipse depth of 100%, the measured transit depth (see Sect. 9) puts an upper limit on the magnitude of a putative eclipsing binary within the photometric aperture, since a fainter source would be overly diluted by the flux from π Men. As the *Gaia* G_{RP} band-pass is a good approximation to the TESS band-pass, we find a limiting magnitude of $G_{RP,max} = 14.1$ mag. Assuming an aperture radius of 60″ (120″), a simulated stellar population along the line of sight to π Men from TRILEGAL[4] (Girardi et al. 2005) implies a frequency of 0.3578 (1.4312) stars brighter than $G_{RP,max}$. Indeed, only one other *Gaia* DR2 source within 2′ of π Men is brighter than $G_{RP,max}$, consistent with the expectation from TRILEGAL: *Gaia* DR2 4623036143819289344 ($G_{RP} = 12.1644 \pm 0.0011$ mag, separation ≈118″). As this source is clearly outside of the TESS photometric aperture, we conclude that π Men is the true host of the transit signal as seen by TESS, and that photometric dilution from sources other than π Men is negligible.

4. Custom light curve preparation

Having established that π Men is the host of the transit signal based on the above analysis of the SPOC aperture and the corresponding light curve, we then performed an analysis of the TESS pixel data by downloading the target pixel file (TPF) for π Men from the MAST web page[5]. We extracted a series of light curves from the pixel data by producing aperture masks containing different contiguous sets of pixels centered on π Men, which appeared elongated due to CCD blooming preferentially along the columns of the detector. The apertures were produced by computing the 50th to 95th percentiles of the median image and selecting pixels with median counts above each percentile value. We then selected an optimal aperture by minimizing the

[2] Available at http://archive.stsci.edu/cgi-bin/dss_form

[3] Available at https://mast.stsci.edu/portal/Mashup/Clients/Mast/Portal.html

[4] Available at http://stev.oapd.inaf.it/cgi-bin/trilegal

[5] Available at https://archive.stsci.edu/prepds/tess-data-alerts/

6.5 h combined differential photometric precision (CDPP) noise metric (Christiansen et al. 2012). We found that the light curves exhibited elevated noise levels between BJD−2450000 ≈ 8347–8350, which corresponded to a deviation in spacecraft pointing. As no transits occur during this time we decided to mask it from each light curve before computing the value of the CDPP noise metric. An aperture somewhat larger than the SPOC aperture yielded the light curve with the best CDPP value, and we use this for our subsequent transit analysis. We note that, although our custom aperture is larger than the SPOC aperture, π Men is so much brighter than other nearby stars that photometric dilution remains negligible compared to the uncertainties of the data.

5. UCLES and HARPS archival spectra

Jones et al. (2002) reported on the detection of a long-period ($P_{\rm orb} \approx 2100$ days), eccentric ($e \approx 0.6$), sub-stellar companion to π Men with a minimum mass of $M_{\rm b} \approx 10\,M_{\rm Jup}$. Their discovery is based on 28 RV measurements obtained between November 1998 and April 2002 using the UCLES spectrograph mounted at the 3.92-m Anglo-Australian Telescope at Siding Spring Observatory. Fourteen additional UCLES RVs taken between August 2002 and October 2005 were published by Butler et al. (2006). For the sake of clarity, we list the 42 UCLES RVs in Table A.1.

We also retrieved from the ESO public archive 145 high-resolution ($R \approx 115\,000$) spectra of π Men, taken with the HARPS spectrograph (Mayor et al. 2003) mounted at the ESO-3.6m telescope of La Silla observatory (Chile). The observations were carried out between 28 December 2012 and 17 March 2017 UTC, as part of the observing programs 072.C-0488, 183.C-0972, and 192.C-0852. The retrieved data-set includes Echelle and order-merged spectra in flexible image transport system (FITS) format, along with additional FITS files containing the cross-correlation function (CCF) and its bisector, computed from the HARPS pipeline using a G2 numerical mask. From the FITS headers, we extracted the barycentric Julian dates, the RVs, and their uncertainties, along with the full width at half maximum (FWHM) and bisector span (BIS) of the CCF, and the S/N per pixel at 5500 Å. On June 2015, the HARPS fiber bundle was upgraded (Lo Curto et al. 2015). To account for the RV offset caused by the instrument refurbishment, we treated the HARPS RVs taken before/after June 2015 as two different data sets (Tables A.2 and A.3). Following Eastman et al. (2010), we converted the heliocentric Julian dates (HJD $_{\rm UTC}$) of the UCLES time stamps and the barycentric Julian (BJD $_{\rm UTC}$) of the HARPS time stamps into barycentric Julian dates in barycentric dynamical time (BJD $_{\rm TDB}$).

6. Stellar fundamental parameters

We determined the spectroscopic parameters of π Men from the co-added HARPS spectrum, which has a S/N per pixel of ∼1880 at 5500 Å. We used Spectroscopy Made Easy (`SME`; Valenti & Piskunov 1996; Valenti & Fischer 2005; Piskunov & Valenti 2017), a spectral analysis tool that calculates synthetic spectra and fits them to high-resolution observed spectra using a χ^2 minimizing procedure. The analysis was performed with the non-LTE `SME` version 5.2.2, along with `ATLAS 12` one-dimensional model atmospheres (Kurucz 2013).

In order to estimate the micro-turbulent ($v_{\rm mic}$) and macro-turbulent ($v_{\rm mac}$) velocities, we used the empirical calibration equations for Sun-like stars from Bruntt et al. (2010) and Doyle et al. (2014), respectively. The effective temperature $T_{\rm eff}$ was measured fitting the wings of the H_α line (Fuhrmann et al. 1993, 1994, 1997a,b; Axer et al. 1994). We excluded the core of H_α because of its origin in higher layers of stellar photospheres. The surface gravity $\log g_\star$ was determined from the wings of the Ca I λ 6102, λ 6122, λ 6162 Å triplet, and the Ca I λ 6439 Å line. We measured the iron abundance [Fe/H] and projected rotational velocity $v \sin i_\star$ by simultaneously fitting the unblended iron lines in the spectral region 5880–6600 Å.

We found an effective temperature of $T_{\rm eff} = 5870 \pm 50$ K, surface gravity $\log g_\star = 4.33 \pm 0.09$ (cgs), and an iron abundance relative to solar of [Fe/H] = 0.05 ± 0.09 dex. We measured a [Ca/H] abundance of 0.07 ± 0.10 dex. The projected rotational velocity was found to be $v \sin i_\star = 3.3 \pm 0.5$ km s^{-1}, with $v_{\rm mic} = 1.06 \pm 0.10$ km s^{-1} and $v_{\rm mac} = 3.35 \pm 0.4$ km s^{-1}. These values were confirmed by modeling the Na I doublet at 5889.95 and 5895.924 Å. We detected no interstellar sodium, as expected given the vicinity of the star (d = 18.3 pc).

We used the BAyesian STellar Algorithm (`BASTA`, Silva Aguirre et al. 2015) with a large grid of `GARSTEC` stellar models (Weiss & Schlattl 2008) to derive the fundamental parameters of π Men. We built the spectral energy distribution (SED) of the star using the magnitudes listed in Table 1, and then fitted the SED along with our spectroscopic parameters ($T_{\rm eff}$, $\log g_\star$, [Fe/H]) and *Gaia* parallax to a grid of `GARSTEC` models. Following Luri et al. (2018), we quadratically added 0.1 mas to the nominal uncertainty of *Gaia* parallax to account for systematic uncertainties of *Gaia* astrometry. We adopted a minimum uncertainty of 0.01 mags for the *Gaia* magnitudes to account for systematic uncertainties in the *Gaia* photometry. Given the proximity of the star (d = 18.3 pc), we assumed no interstellar reddening.

We found that π Men has a mass of $M_\star = 1.02 \pm 0.03\ M_\odot$ and a radius of $R_\star = 1.10 \pm 0.01\ R_\odot$, implying a surface gravity of $\log g_\star = 4.36 \pm 0.02$ (cgs), in agreement with the spectroscopically derived value of 4.33 ± 0.09. The stellar models constrain the age of the star to be 5.2 ± 1.1 Gyr. The fundamental parameters of π Men are given in Table A.4. We stress that the uncertainties on the derived parameters are internal to the stellar models used and do not include systematic uncertainties related to input physics or to the bolometric correction.

7. Seismic analysis

In order to better characterize the star, we performed an asteroseismic analysis of the SPOC light curve as well as the custom light curve optimized for characterization of the exoplanet (Sect. 4). For the former, the corrections we made consist of three steps. First, we corrected the SPOC flux[6] performing a robust locally weighted regression as described in Cleveland (1979) in order to smooth long-period variation from the light curve without removing any transit signal. We also calibrated the data following the methods described in García et al. (2011). The results of both analyses provided similar seismic results, although the corrections applied were very different. As a second step we removed the transits by folding the light curve at the period of the planet transit and filtering it with a wavelet transform using an "à trous" algorithm (Starck & Murtagh 2002, 2006). Finally as the last step, the gaps of the resultant light curve were interpolated using inpainting techniques following García et al. (2014) and Pires et al. (2015). For the custom

[6] We used the pre-search data conditioning simple aperture photometry (Smith et al. 2012).

aperture (Sect. 4), the first step consisted of correcting the light curve following only García et al. (2011) (as the two corrections methods led to similar results) and we applied the same steps two and three.

We used the FliPer metric (Bugnet et al. 2018) to estimate $\log g_\star$ directly from the global power of the power spectrum density of both light curves. Unfortunately, due to the high level of noise and the filters applied to the light curve to flatten it and properly remove the transits, part of the power below ~100 μHz is removed providing only a loose limit of the value of surface gravity or the frequency of maximum power of the modes. We applied the standard seismic A2Z pipeline (Mathur et al. 2010) to look for the power excess due to acoustic modes. While the blind search did not yield a significant detection in either light curve, we estimated where we would expect the acoustic modes given the spectroscopic parameters derived in this paper. The modes are expected around 2500 μHz. The power spectrum of SPOC light curve shows a slight excess of power around 2600 μHz (frequency of maximum power or $\nu_{\rm max}$) and the A2Z pipeline that computes the power spectrum of the power spectrum detects a signal at 119.98 ± 9.25 μHz, which could be the large frequency separation ($\Delta\nu$ is the frequency difference between 2 modes of same degree and consecutive orders) with a 95% confidence level. This value corresponds to the $\Delta\nu$ expected from the global seismic scaling relations for modes at 2607 ± 16 μHz. Although quite unlikely, this signal could be due to noise. If we consider that this is a real seismic signature, using $\Delta\nu$, $\nu_{\rm max}$, and $T_{\rm eff}$, along with the solar scaling relations, we found a stellar mass of $M_\star = 1.02 \pm 0.15\, M_\odot$ and a stellar radius of $R_\star = 1.09 \pm 0.10\, R_\odot$, in agreement with the spectroscopic values (Sect. 6). However, the asteroseismic analysis of the custom light curve does not reproduce the previous results, as the seismic signal is not statistically significant. A better knowledge of the optimal aperture mask for asteroseismology is required at this point, which is beyond the scope of this paper. We note that this marginal detection is expected for a star of this magnitude and evolutionary stage observed over the course of one month. Asteroseismic analysis with TESS will require multiple-sector data and/or more evolved bright stars, as predicted by pre-launch simulations (Campante 2017).

8. Frequency analysis of the Doppler data

We performed a frequency analysis of the UCLES and HARPS RVs in order to search for the presence of the transiting planet in the Doppler data, and look for possible additional periodic signals. The generalized Lomb-Scargle (GLS; Zechmeister & Kürster 2009) periodogram of the combined UCLES and HARPS RVs[7] shows a very significant peak at the orbital frequency of the outer sub-stellar companion ($f_b = 0.0005$ c/d), with a false-alarm probability (FAP) lower than 10^{-10}.

The upper panel of Fig. 2 displays the GLS periodogram of the RV residuals following the subtraction of the Doppler signal induced by the outer sub-stellar object. We found that the most significant peak is seen at the frequency of the transit signal detected by TESS ($f_c = 0.16$ c/d), with a FAP $< 10^{-5}$ and an RV semi-amplitude of ~1.5 m s^{-1}. The peak has no counterparts in the periodograms of the HARPS activity indicators (second and third panels of Fig. 2), suggesting that the signal is induced by the presence of an orbiting planet with a period of 6.27 days.

[7] We accounted for the instrumental offsets using the values derived in Sect. 9.

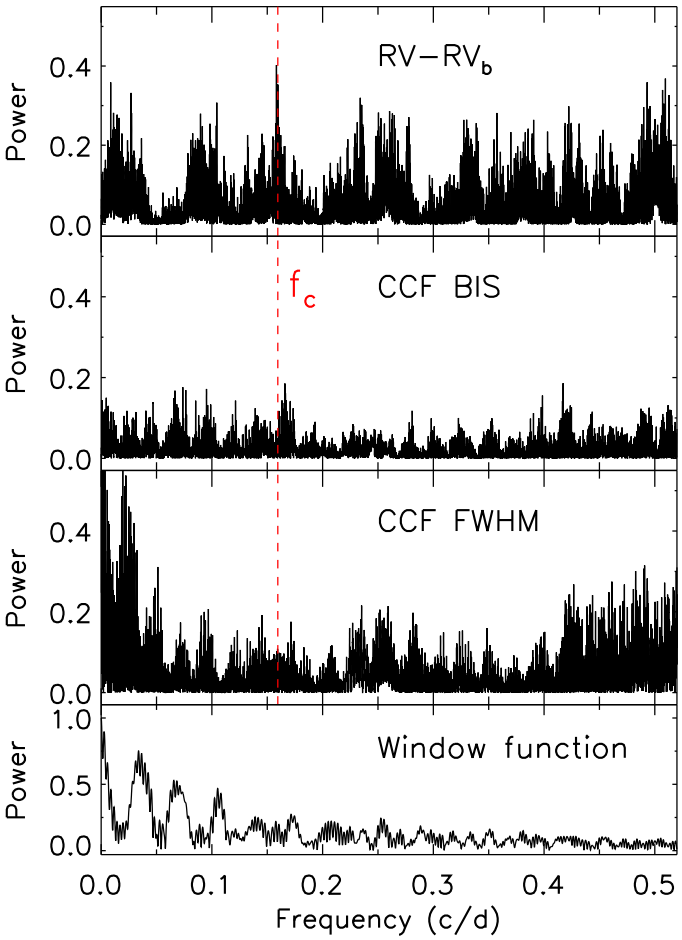

Fig. 2. *First panel*: GLS periodogram of the UCLAS and HARPS RV residuals following the subtraction of the Doppler reflex motion induced by the outer sub-stellar companion. *Second and third panels*: GLS periodogram of the BIS and FWHM of the HARPS CCF (data acquired with the old fiber bundle). *Fourth panel*: periodogram of the window function of the combined RV measurements. The dashed vertical red line marks the orbital frequency of the transiting planet ($f_c = 0.16$ c/d).

We also subtracted the Doppler reflex motion induced by the transiting planet from our RV data and searched the residuals for additional periodic signal but found no peak with FAP $< 10^{-4}$.

9. Joint analysis of the transit and Doppler data

We performed a joint analysis of our custom light curve (Sect. 4) and RV measurements (Sect. 5) using the software suite `pyaneti` (Barragán et al. 2019), which allows for parameter estimation from posterior distributions calculated using Markov chain Monte Carlo methods.

We extracted 10 h of TESS data points centered around each of the five transits observed by TESS. The five segments were de-trended using the code `exotrending` (Barragán & Gandolfi 2017), fitting a second-order polynomial to the out-of-transit data. We used all 187 Doppler measurements presented in Sect. 5 and accounted for the RV offsets between the different instruments and the two HARPS setups.

The RV model consists of two Keplerians to account for the Doppler signal induced by planets *b* and *c*. We fitted for a RV jitter term for each instrument/setup to account for instrumental noise not included in the nominal uncertainties, and/or to account for any stellar-activity-induced RV variation. We

modeled the TESS transit light curves using the limb-darkened quadratic model of Mandel & Agol (2002). For the limb darkening coefficients, we set Gaussian priors using the values derived by Claret (2017) for the TESS pass-band. We imposed conservative error bars of 0.1 on both the linear and the quadratic limb-darkening term. A preliminary analysis showed that the transit light curve poorly constrains the scaled semi-major axis ($a/R_\star$). We therefore set a Gaussian prior on $a/R_\star$ using Kepler's third's law, the orbital period, and the derived stellar parameters (Sect. 6). Because the eccentricity of planet *c* is poorly constrained by the observations, we fixed it to zero for our analysis (see also Sect. 10). We imposed uniform priors for the remaining fitted parameters. Details of the fitted parameters and prior ranges are given in Table A.4. Before performing the final analysis, we ran a numerical experiment to check if the TESS two-minute integration time needed to be taken into account following Kipping (2010). We found no differences in the posterior distributions for fits with and without re-sampling; we therefore proceeded with our analysis without re-sampling. We used 500 independent Markov chains initialized randomly inside the prior ranges. Once all chains converged, we used the last 5000 iterations and saved the chain states every ten iterations. This approach generates a posterior distribution of 250 000 points for each fitted parameter. Table A.4 lists the inferred planetary parameters. They are defined as the median and 68% region of the credible interval of the posterior distributions for each fitted parameter. The transit and RV curves are shown in Fig. 3.

10. Discussion and conclusion

π Men is a bright ($V = 5.65$ mag) Sun-like star (SpT = G0 V) known to host a sub-stellar companion (π Men b) on a long-period eccentric orbit (Jones et al. 2002). Combining *Gaia* photometry with archival RV measurements we confirmed that the $P = 6.27$ day transit signal detected in the TESS light curve of π Men is caused by a bona fide transiting super-Earth and derived its mass. π Men c becomes TESS's first confirmed planet.

π Men joins the growing number of stars known to host both long-period Jupiter analogs and close-in small planets ($R_\mathrm{p} < 4\,R_\oplus$). Zhu & Wu (2018) pointed out that long-period, gas-giant planets are common around stars hosting super-Earths. Bryan et al. (2018) recently found that the occurrence rate of companions in the range 0.5–20 M_Jup at 1–20 AU in systems known to host inner small planets is 39 ± 7%, suggesting that the presence of outer gas giant planets does not prevent the formation of inner Earth- and Neptune-size planets. We performed a dynamical stability analysis of π Men using the software `mercury6` (Chambers 1999). Assuming co-planar orbits, we let the system evolve for 100 000 yr. For π Men b we found negligible changes of the semi-major axis and eccentricity of $<2.6\times10^{-3}$ AU and 3×10^{-4}, respectively. For π Men c we found no variation larger than 1×10^{-5} of its semi-major axis, with changes of its eccentricity $\lesssim 0.05$.

The actual orientation of the outer planet's orbit is unknown. While we know the inner planet's inclination, because it transits, its eccentricity is poorly constrained by the data. Compact multi-planet systems have been observed to have near-zero eccentricities (e.g., Hadden & Lithwick 2014; Van Eylen & Albrecht 2015; Xie et al. 2016). However, planets with only a single transiting planet often appear to be "dynamically hotter", and many have a non-zero eccentricity, which can, for example, be described by the positive half of a zero-mean Gaussian distribution, with a dispersion $\sigma_\mathrm{e} = 0.32 \pm 0.06$ (Van Eylen et al. 2018b). The outer planet, π Men c, has an orbital eccentricity of ~0.64.

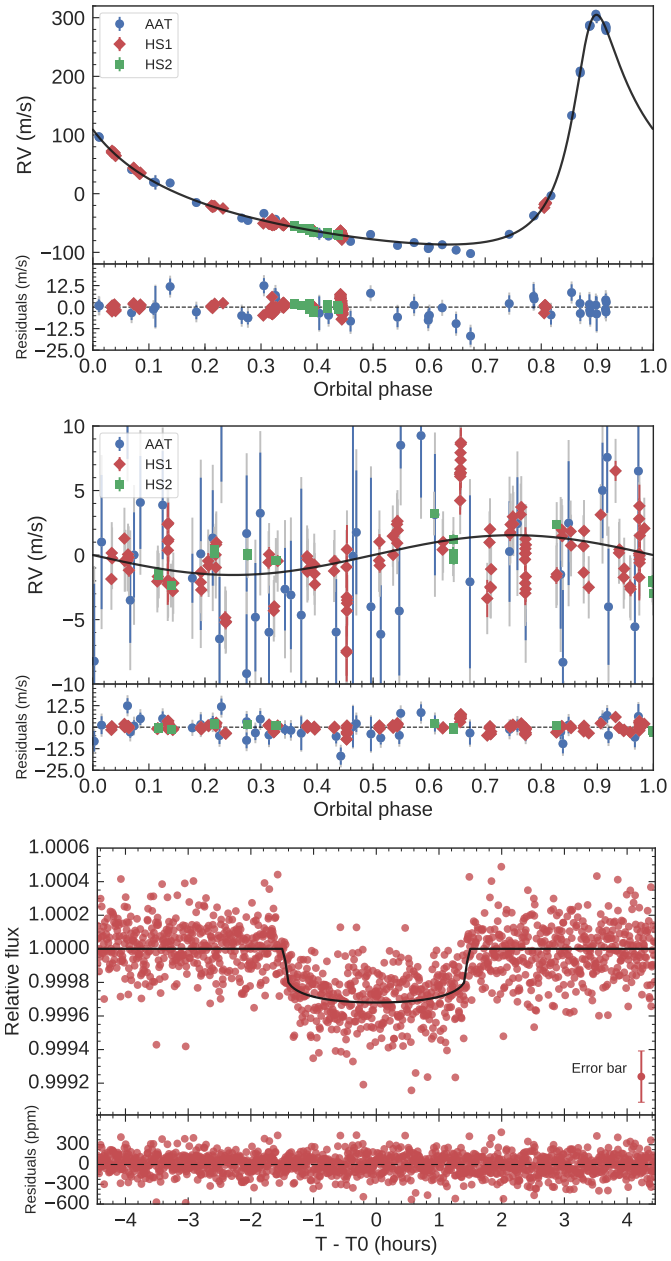

Fig. 3. Phase-folded RV curves of π Men b (*upper panel*) and c (*middle panel*), and transit light curve of π Men c (*lower panel*). The best-fitting transit and Keplerian models are overplotted with thick black lines. The zero phases of the RV curves of π Men b (*upper panel*) and c (*lower panel*) correspond to the time of inferior conjunction and transit epoch, respectively (Table A.4). The TESS data points are shown with red circles (*lower panel*). The AAT data and the two sets of HARPS RVs (HS1 and HS2) are shown with circles, diamonds, and squares, respectively. The vertical gray lines mark the error bars including jitter.

A far-out giant planet, such as planet *c*, may in fact increase the orbital eccentricity of a close-in super-Earth, such as planet *b* (see, e.g., Mustill et al. 2017; Hansen 2017; Huang et al. 2017). Following Van Eylen et al. (2018b), we found an orbital eccentricity based on the transit data alone of $[0, 0.45]$ at 68% confidence. Because the current RV observations cannot constrain the eccentricity either, we fixed it to zero in the above analysis (see Sect. 9). The brightness of the host star makes this planetary system an exciting target for further RV follow-up to measure the inner planet's eccentricity.

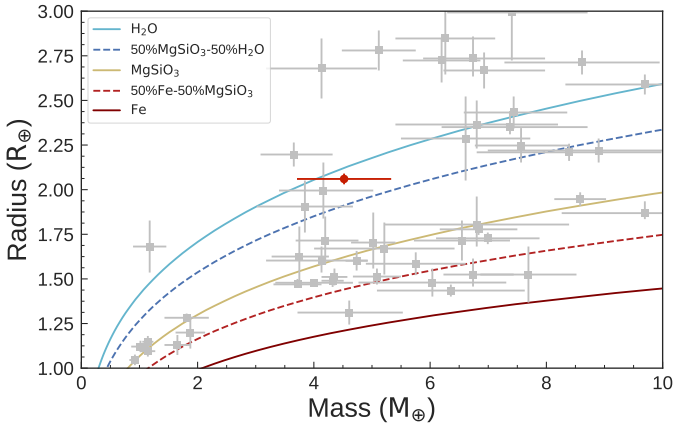

Fig. 4. Mass-radius for low-mass ($M_p < 10\ M_\oplus$), small ($R_p < 3\ M_\oplus$) planets with mass-radius measurements better than 25% (from http://www.astro.keele.ac.uk/jkt/tepcat/; Southworth et al. 2007). Composition models from Zeng et al. (2016) are displayed with different lines and colors. The solid red circle marks the position of π Men c.

The transiting planet π Men c has a mass of $M_c = 4.52 \pm 0.81\ M_\oplus$ and a radius of $R_c = 2.06 \pm 0.03\ R_\oplus$, yielding a mean density of ρ_c=2.82 ± 0.53 g cm^{-3}. Figure 4 shows the mass-radius diagram for small planets whose masses have been determined with a precision better than 25 %. Theoretical models from Zeng et al. (2016) are overplotted using different lines and colors. The position of π Men c suggests a composition of Mg silicates and water. Alternatively, the planet might have a solid core surrounded by a gas envelope. At short orbital periods, super-Earths and sub-Neptunes are separated by a radius gap at $\approx 1.8\ R_\oplus$ (Fulton et al. 2017; Van Eylen et al. 2018a). The exact location of the radius gap is observed to be a function of the orbital period (Van Eylen et al. 2018a), as predicted by models of photo-evaporation (e.g., Owen & Wu 2013; Lopez & Fortney 2013). Van Eylen et al. (2018a) found that the radius gap is located at $\log R = m \times \log P + a$, where $m = -0.09^{+0.02}_{-0.04}$ and $a = 0.37^{+0.04}_{-0.02}$. At the orbital period of π Men c, that is, P_{orb} = 6.27 days, the radius gap is then located at $R_p = 1.99 \pm 0.20\ R_\oplus$. This implies that π Men c, with a radius of $R_c = 2.06 \pm 0.03\ R_\oplus$, is located just around the radius gap, although the measured density suggests that the planet may have held on to (part of) its atmosphere.

The naked-eye brightness of π Men immediately argues that any transiting planet will be attractive for atmospheric characterization. Observations of a planetary atmosphere through transmission spectroscopy during transit provide opportunities to measure the extent, kinematics, abundances, and structure of the atmosphere (Seager & Deming 2010). Such measurements can be utilized to address fundamental questions such as planetary atmospheric escape and interactions with the host star (Cauley et al. 2017), formation and structure of planetary interiors (Owen et al. 1999), planetary and atmospheric evolution (Öberg et al. 2011), and biological processes (Meadows et al. 2010).

The left panel of Fig. 5 displays a relative atmospheric detection S/N metric normalized to π Men c for all known small exoplanets with $R_p < 3\ R_\oplus$. The sample is taken from the Exoplanet Orbit Database[8] as of September 2018. The atmospheric signal is calculated in a similar way to Gillon et al. (2016) and Niraula et al. (2017). In particular, the relative atmospheric S/N plotted in Fig. 5 is calculated from Eqs. (1a) and (1b) from Niraula et al. (2017). This calculation assumes similar atmospheric properties (e.g., Bond albedo, mean molecular weight) for all planets. Large atmospheric signals result from hot, extended atmospheres of planets that transit small, cool stars. For this reason, planets transiting such stars as GJ 1214 and TRAPPIST-1 are excellent targets for this kind of study. Nevertheless, the brightness of the host star along with the period and duration of the transit also significantly contribute to the ability to build up a sufficiently high S/N to detect atmospheric signals. We used the J-band flux (e.g., H_2O measurements with JWST; Beichman et al. 2014) and weighted the metric to optimize the S/N over a period of time rather than per transit.

In the context of all small planets ($R_p < 3\ R_\oplus$), π Men c has the seventh strongest atmospheric signal, behind GJ 1214 b, 55 Cnc e, the TRAPPIST-1 b and c planets, HD219134 b, and Kepler-42 c. However, π Men is unique among this notable group of stars in that it is the only G-type star (Fig. 5, right panel). All of the other exoplanets transit K- or M-type stars. The brightness of π Men is able to overcome the disadvantage of a small planet transiting a slightly larger star, to provide the best opportunity of probing the atmospheric properties of a super-Earth orbiting a solar type star. Given the significant changes in the structure of stellar coronae and stellar winds between G- and M-type stars, the atmospheric properties and evolution of π Men c may be distinctly different from the atmospheres detected around the sample of very-low-mass M-type stars (e.g., GJ 1214 and TRAPPIST-1). For example, the TRAPPIST-1 e, f, and g planets essentially orbit within the stellar corona of the host star and may be subject to a substantial stellar wind, which will result in a strong injection of energy in the atmosphere and may prevent the formation of a significant atmosphere (Cohen et al. 2018). When inferring the properties of coronae and winds of stars other than the Sun, we often have to use poorly constrained models and empirical correlations, the validity of which are best for stars that are quite similar to the Sun. In this respect, π Men is a unique laboratory because of its greater similarities to the Sun with respect to all the other stars known to host mini-Neptunes and Super-Earths amenable to multi-wavelength atmospheric characterization.

We further studied the long-term stability of a possible hydrogen-dominated atmosphere by estimating the mass-loss rates. To this end, we employed the interpolation routine described by Kubyshkina et al. (2018), which interpolates the mass-loss rate among those obtained with a large grid of one-dimensional upper-atmosphere hydrodynamic models for super-Earths and sub-Neptunes. Employing the values listed in Table A.4 and a Sun-like high-energy emission, which is a reasonable assumption given that π Men has a temperature and age similar to those of the Sun, we obtained a mass-loss rate of 1.2×10^{10} g s^{-1}, which corresponds to ~1.4% of the estimated planetary mass per gigayear. This indicates that the question of whether the planet still holds a hydrogen-dominated atmosphere or not greatly depends on the initial conditions, namely how much hydrogen the planet accreted during its formation. If the planet originally accreted a small hydrogen-dominated atmosphere with a mass of only a few percent of the total planetary mass, we can expect it to be, for the vast majority, lost, particularly taking into account that the star was more active in the past. In contrast, a significant hydrogen mass fraction would still be present if the planet originally accreted a large amount of hydrogen. The inferred bulk density hints at the possible presence of a hydrogen-dominated atmosphere, but it does not give a clear indication. Ultraviolet observations aiming at detecting hydrogen Ly$_\alpha$ absorption and/or carbon and oxygen in the upper

[8] Available at http://exoplanets.org

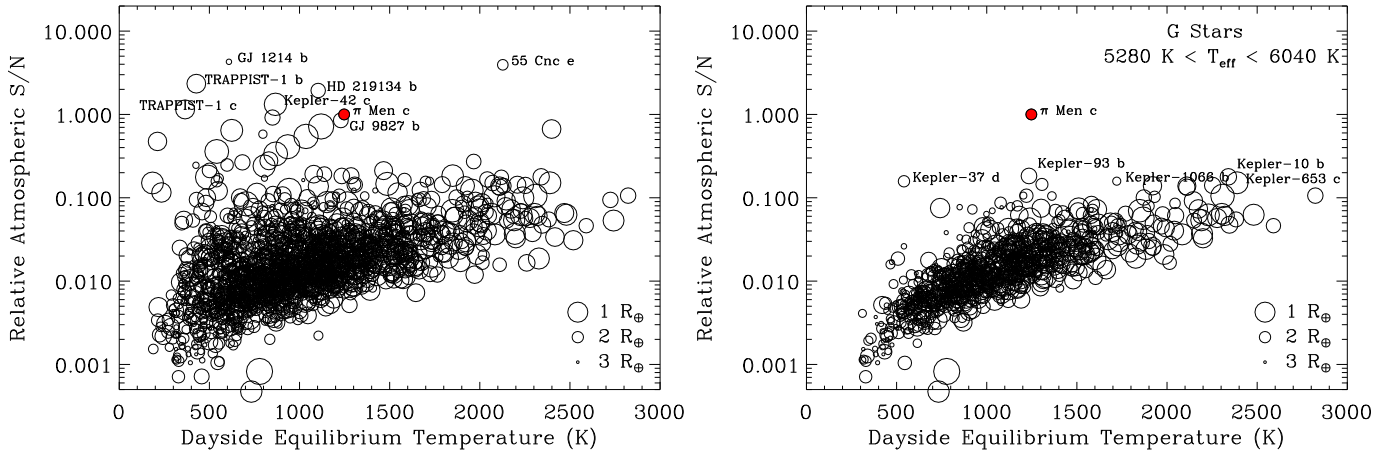

Fig. 5. *Left panel*: relative S/N of an atmospheric signal for all exoplanets with $R_p < 3\,R_\oplus$ as a function of planetary equilibrium temperature. The symbol size is inversely proportional to the planetary radius, emphasizing those closest to an Earth radius. The π Men c planet is used as the atmospheric signal reference and it is indicated by the filled circle. It is among the top ten most favorable planets for atmospheric characterization. *Right panel*: as in the left panel, simply limited to solar type host stars (i.e., G-type stars; $5280 < T_{\rm eff} < 6040$ K). The π Men c planet is by far the most favorable planet around such a star for atmospheric characterization. The other optimal atmospheric targets all transit K and M stars. For this reason, the coronal and stellar wind properties that interact with the π Men c atmosphere may be distinctly different to those experienced by the rest of the sample.

planetary atmosphere would be decisive in identifying its true nature.

While this manuscript was in preparation, Huang et al. (2018) publicly reported an independent analysis of the π Men system, using a custom TESS photometry pipeline. They measured a mass and radius for π Men c consistent within less than 1-σ with our measurements.

Acknowledgements. Davide Gandolfi is lovingly grateful to Conny Konnopke for her unique support during the preparation of this paper, and her valuable suggestions and comments. J.H.L. gratefully acknowledges the support of the Japan Society for the Promotion of Science (JSPS) Research Fellowship for Young Scientists. M.F. and C.M.P. gratefully acknowledge the support of the Swedish National Space Board. A.P.H., Sz.Cs., S.G., J.K., M.P., and M.E. acknowledge support by DFG (Deutsche Forschungsgemeinschaft) grants HA 3279/12-1, PA525/18-1, PA525/19-1, PA525/20-1, and RA 714/14-1 within the DFG Schwerpunkt SPP 1992, "Exploring the Diversity of Extrasolar Planets." S.M acknowledges support from the Ramon y Cajal fellowship number RYC-2015-17697. We acknowledge the use of TESS Alert data, which is currently in a beta test phase, from pipelines at the TESS Science Office and at the TESS Science Processing Operations Center. Funding for the TESS mission is provided by NASA's Science Mission directorate. Based on observations made with the ESO 3.6m telescope at La Silla Observatory under programme ID 072.C-0488, 183.C-0972, and 192.C-0852. This work has made use of data from the European Space Agency (ESA) mission *Gaia* (https://www.cosmos.esa.int/gaia), processed by the *Gaia* Data Processing and Analysis Consortium (DPAC, https://www.cosmos.esa.int/web/gaia/dpac/consortium). Funding for the DPAC has been provided by national institutions, in particular the institutions participating in the *Gaia* Multilateral Agreement. We acknowledge the traditional owners of the land on which the AAT stands, the Gamilaraay people, and pay our respects to elders past and present. We are also very grateful to the referee, Steve Howell, for his helpful comments and suggestions, which resulted in an improved paper. We also thank him for his rapid review of the paper.

References

Axer, M., Fuhrmann, K., & Gehren, T. 1994, A&A, 291, 895
Barragán, O., & Gandolfi, D. 2017, Astrophysics Source Code Library [record ascl:1706.001]
Barragán, O., Gandolfi, D., & Antoniciello, G. 2019, MNRAS, 482, 1017
Beichman, C., Benneke, B., Knutson, H., et al. 2014, PASP, 126, 1134
Bruntt, H., Bedding, T. R., Quirion, P.-O., et al. 2010, MNRAS, 405, 1907
Bryan, M. L., Knutson, H. A., & Fulton, B., et al. 2018, AJ, submitted [arXiv:1806.08799]
Bugnet, L., García, R. A., Davies, G. R., et al. 2018, A&A, in press, DOI: 10.1051/0004-6361/201833106
Butler, R. P., Wright, J. T., Marcy, G. W., et al. 2006, ApJ, 646, 505
Campante, T. L. 2017, Eur. Phys. J. Web Conf. , 160, 01006
Cauley, P. W., Redfield, S., & Jensen, A. G. 2017, AJ, 153, 185
Chambers, J. E. 1999, MNRAS, 304, 793
Christiansen, J. L., Jenkins, J. M., Caldwell, D. A., et al. 2012, PASP, 124, 1279
Claret, A. 2017, A&A, 600, A30
Cleveland, W. S. 1979, J. Am. Stat. Assoc., 74, 829
Cohen, O., Glocer, A., Garraffo, C., Drake, J. J., & Bell, J. M. 2018, ApJ, 856, L11
Cutri, R. M., Skrutskie, M. F., & van Dyk, S., et al. 2003, 2MASS All Sky Catalog of point sources
Doyle, A. P., Davies, G. R., Smalley, B., Chaplin, W. J., & Elsworth, Y. 2014, MNRAS, 444, 3592
Eastman, J., Siverd, R., & Gaudi, B. S. 2010, PASP, 122, 935
Fuhrmann, K., Axer, M., & Gehren, T. 1993, A&A, 271, 451
Fuhrmann, K., Axer, M., & Gehren, T. 1994, A&A, 285, 585
Fuhrmann, K., Pfeiffer, M., Frank, C., Reetz, J., & Gehren, T. 1997a, A&A, 323, 909
Fuhrmann, K., Pfeiffer, M. J., & Bernkopf, J. 1997b, A&A, 326, 1081
Fulton, B. J., Petigura, E. A., Howard, A. W., et al. 2017, AJ, 154, 109
Gaia Collaboration (Brown, A. G. A., et al.) 2018, A&A, 616, A1
García, R. A., Hekker, S., Stello, D., et al. 2011, MNRAS, 414, L6
García, R. A., Mathur, S., Pires, S., et al. 2014, A&A, 568, A10
Gillon, M., Jehin, E., Lederer, S. M., et al. 2016, Nature, 533, 221
Girardi, L., Groenewegen, M. A. T., Hatziminaoglou, E., & da Costa, L. 2005, A&A, 436, 895
Gray, R. O., Corbally, C. J., Garrison, R. F., et al. 2006, AJ, 132, 161
Hadden, S., & Lithwick, Y. 2014, ApJ, 787, 80
Hansen, B. M. S. 2017, MNRAS, 467, 1531
Huang, C. X., Petrovich, C., & Deibert, E. 2017, AJ, 153, 210
Huang, C. X., Burt, J., Vanderburg, A., et al. 2018, ApJL, accepted [arXiv:1809.05967]
Jones, H. R. A., Paul Butler, R., Tinney, C. G., et al. 2002, MNRAS, 333, 871
Kipping, D. M. 2010, MNRAS, 408, 1758
Kovács, G., Zucker, S., & Mazeh, T. 2002, A&A, 391, 369
Kubyshkina, D., Fossati, L., Erkaev, N.V., et al. 2018, ArXiv e-prints [arXiv:1809.06645]
Kurucz, R. L. 2013, Astrophysics Source Code Library [record ascl:1303.024]
Lo Curto, G., Pepe, F., Avila, G., et al. 2015, The Messenger, 162, 9
Lopez, E. D., & Fortney, J. J. 2013, ApJ, 776, 2
Luri, X., Brown, A. G. A., Sarro, L. M., et al. 2018, A&A, 616, A9
Mandel, K., & Agol, E. 2002, ApJ, 580, L171
Mathur, S., García, R. A., Régulo, C., et al. 2010, A&A, 511, A46
Mayor, M., Pepe, F., Queloz, D., et al. 2003, The Messenger, 114, 20
Meadows, V., & Seager, S. 2010, in Terrestrial Planet Atmospheres and Biosignatures, ed. S. Seager, 441

Mermilliod, J.-C. 1987, A&AS, 71, 413
Mustill, A. J., Davies, M. B., & Johansen, A. 2017, MNRAS, 468, 3000
Niraula, P., Redfield, S., Dai, F., et al. 2017, AJ, 154, 266
Öberg, K. I., Murray-Clay, R., & Bergin, E. A. 2011, ApJ, 743, L16
Owen, J. E., & Wu, Y. 2013, ApJ, 775, 105
Owen, T., Mahaffy, P., Niemann, H. B., et al. 1999, Nature, 402, 269
Pires, S., Mathur, S., García, R. A., et al. 2015, A&A, 574, A18
Piskunov, N., & Valenti, J. A. 2017, A&A, 597, A16
Ricker, G. R., Winn, J. N., Vanderspek, R., et al. 2015, J. Astron. Telescopes Instrum. Syst., 1, 014003
Seager, S., & Deming, D. 2010, ARA&A, 48, 631
Silva Aguirre, V., Davies, G. R., Basu, S., et al. 2015, MNRAS, 452, 2127
Smith, J. C., Stumpe, M. C., Van Cleve, J. E., et al. 2012, PASP, 124, 1000
Southworth, J., Wheatley, P. J., & Sams, G. 2007, MNRAS, 379, L11
Starck, J. L., & Murtagh, F. 2002, Astronomical Image and Data Analysis (Berlin: Springer)
Starck, J. L., & Murtagh, F. 2006, Astronomical Image and Data Analysis (Berlin Heidelberg: Springer-Verlag)
Stassun, K. G., Oelkers, R. J., Pepper, J., et al. 2018, AJ, 156, 102
Valenti, J. A., & Fischer, D. A. 2005, ApJS, 159, 141
Valenti, J. A., & Piskunov, N. 1996, A&AS, 118, 595
Van Eylen, V., & Albrecht, S. 2015, ApJ, 808, 126
Van Eylen, V., Agentoft, C., Lundkvist, M. S., et al. 2018a, MNRAS, 479, 4786
Van Eylen, V., Albrecht, S., & Huang, X., et al. 2018b, AAS, submitted [arXiv:1807.00549]
Weiss, A., & Schlattl, H. 2008, Ap&SS, 316, 99
Xie, J.-W., Dong, S., Zhu, Z., et al. 2016, Proc. Nat. Acad. Sci., 113, 11431
Zechmeister, M., & Kürster, M. 2009, A&A, 496, 577
Zeng, L., Sasselov, D. D., & Jacobsen, S. B. 2016, ApJ, 819, 127
Zhu, W., & Wu, Y. 2018, AJ, 156, 92

[1] Dipartimento di Fisica, Università degli Studi di Torino, Via Pietro Giuria 1, 10125 Torino, Italy
e-mail: davide.gandolfi@unito.it
[2] Department of Astronomy, Graduate School of Science, The University of Tokyo, Hongo 7-3-1, Bunkyo-ku, Tokyo 113-0033, Japan
[3] Department of Space, Earth and Environment, Chalmers University of Technology, Onsala Space Observatory, 439 92 Onsala, Sweden
[4] Leiden Observatory, University of Leiden, PO Box 9513, 2300 RA Leiden, The Netherlands
[5] Stellar Astrophysics Centre, Deparment of Physics and Astronomy, Aarhus University, Ny Munkegrade 120, 8000 Aarhus C, Denmark
[6] Astronomy Department and Van Vleck Observatory, Wesleyan University, Middletown, CT 06459, USA
[7] Space Research Institute, Austrian Academy of Sciences, Schmiedlstrasse 6, 8041 Graz, Austria
[8] Departamento de Astrofísica, Universidad de La Laguna, 38206 Tenerife, Spain
[9] Instituto de Astrofísica de Canarias, C/ Vía Láctea s/n, 38205 La Laguna, Tenerife, Spain
[10] Rheinisches Institut für Umweltforschung, Abteilung Planetenforschung an der Universität zu Köln, Aachener Strasse 209, 50931 Köln, Germany
[11] Institute of Planetary Research, German Aerospace Center, Rutherfordstrasse 2, 12489 Berlin, Germany
[12] IRFU, CEA, Université Paris-Saclay, 91191 Gif-sur-Yvette, France
[13] Université Paris Diderot, AIM, Sorbonne Paris Cité, CEA, CNRS, 91191 Gif-sur-Yvette, France
[14] Department of Astrophysical Sciences, Princeton University, 4 Ivy Lane, Princeton, NJ 08544, USA
[15] Thüringer Landessternwarte Tautenburg, Sternwarte 5, 07778 Tautenberg, Germany
[16] Department of Astronomy and McDonald Observatory, University of Texas at Austin, 2515 Speedway, Stop C1400 Austin, TX 78712, USA

Appendix A: Additional tables

Table A.1. UCLES RV measurements of π Men.

BJD_{TDB}[a] −2450000	RV (km s^{-1})	$\pm\sigma$ (km s^{-1})	BJD_{TDB}[a] −2450000	RV (km s^{-1})	$\pm\sigma$ (km s^{-1})
829.993723	−0.0410	0.0048	2154.305009	0.3030	0.0100
1119.251098	−0.0674	0.0098	2187.196618	0.2857	0.0039
1236.033635	−0.0792	0.0060	2188.236606	0.2893	0.0037
1411.325662	−0.0858	0.0058	2189.223031	0.2797	0.0033
1473.267712	−0.0800	0.0048	2190.145881	0.2835	0.0037
1526.081162	−0.0930	0.0046	2387.871387	0.1009	0.0036
1527.082805	−0.0898	0.0041	2389.852023	0.0974	0.0033
1530.128708	−0.0879	0.0045	2510.307394	0.0417	0.0042
1629.912366	−0.0927	0.0056	2592.126975	0.0202	0.0032
1683.842991	−0.1005	0.0050	2599.155380	0.0210	0.0120
1828.188260	−0.0674	0.0048	2654.099326	0.0188	0.0047
1919.099660	−0.0350	0.0072	2751.918480	−0.0117	0.0042
1921.139081	−0.0373	0.0047	2944.224628	−0.0434	0.0038
1983.919846	−0.0028	0.0056	3004.075458	−0.0321	0.0044
2060.840355	0.1361	0.0048	3042.078745	−0.0440	0.0042
2092.337359	0.2120	0.0047	3043.018085	−0.0463	0.0045
2093.352231	0.2094	0.0044	3047.050110	−0.0408	0.0043
2127.328562	0.2878	0.0059	3048.097508	−0.0444	0.0036
2128.336410	0.2861	0.0042	3245.311649	−0.0697	0.0050
2130.339049	0.2899	0.0067	3402.035747	−0.0669	0.0018
2151.292440	0.3079	0.0052	3669.244092	−0.0863	0.0019

Notes. [a]Barycentric Julian dates are given in barycentric dynamical time.

Table A.2. HARPS RV measurements of π Men acquired with the old fiber bundle.

BJD_{TDB}[a] −2450000	RV (km s^{-1})	$\pm\sigma$ (km s^{-1})	BIS (km s^{-1})	*FWHM* (km s^{-1})	T_{exp} (s)	S/N[b]
3001.830364	10.6600	0.0014	−0.0019	7.6406	109	69.0
3034.607261	10.6665	0.0008	0.0040	7.6368	200	120.7
3289.869718	10.6448	0.0012	−0.0013	7.6378	60	79.6
3289.870782	10.6428	0.0011	−0.0012	7.6406	60	89.4
3289.871836	10.6446	0.0011	−0.0007	7.6394	60	90.7
3289.872866	10.6449	0.0011	−0.0026	7.6439	60	86.5
...	...	...	...	...	...	...

Notes. The entire RV data set is available at the CDS. [a]Barycentric Julian dates are given in barycentric dynamical time. [b]S/N per pixel at 550 nm.

Table A.3. HARPS RV measurements of π Men acquired with the new fiber bundle.

BJD_{TDB}[a] −2450000	RV (km s^{-1})	$\pm\sigma$ (km s^{-1})	BIS (km s^{-1})	*FWHM* (km s^{-1})	T_{exp} (s)	S/N[b]
7298.853243	10.6750	0.0005	0.0081	7.6856	450	187.3
7298.858243	10.6747	0.0004	0.0083	7.6842	450	242.8
7327.755817	10.6744	0.0003	0.0089	7.6870	900	305.7
7354.783687	10.6674	0.0002	0.0104	7.6867	900	538.0
7357.725912	10.6727	0.0002	0.0105	7.6858	900	542.9
7372.705131	10.6664	0.0004	0.0094	7.6825	300	273.0
7372.708997	10.6662	0.0004	0.0118	7.6822	300	247.3
7372.712758	10.6654	0.0003	0.0104	7.6831	300	320.9
7423.591772	10.6630	0.0005	0.0113	7.6796	450	217.1
7423.597918	10.6628	0.0005	0.0115	7.6782	450	214.1
7424.586637	10.6645	0.0004	0.0104	7.6814	450	299.7
7424.592367	10.6643	0.0004	0.0113	7.6816	450	288.5
7462.517924	10.6612	0.0003	0.0116	7.6822	450	326.8
7462.523491	10.6612	0.0003	0.0106	7.6816	450	337.8
7464.499915	10.6616	0.0005	0.0083	7.6812	300	217.7
7464.503781	10.6627	0.0004	0.0112	7.6818	300	276.2
7464.507474	10.6611	0.0004	0.0108	7.6820	300	286.4

Notes. [a]Barycentric Julian dates are given in barycentric dynamical time. [b]S/N per pixel at 550 nm.

Table A.4. π Men system parameters.

Parameter	Prior[a]	Derived value
Stellar parameters		
Star mass $M_\star$ ($M_\odot$)	···	1.02 ± 0.03
Star radius $R_\star$ ($R_\odot$)	···	1.10 ± 0.01
Effective Temperature $T_{\rm eff}$ (K)	···	5870 ± 50
Surface gravity[b] $\log g_\star$ (cgs)	···	4.36 ± 0.02
Surface gravity[c] $\log g_\star$ (cgs)	···	4.33 ± 0.09
Iron abundance [Fe/H] (dex)	···	0.05 ± 0.09
Projected rotational velocity $v \sin i_\star$ (km s^{-1})	···	3.3 ± 0.5
Age (Gyr)	···	5.2 ± 1.1
Model parameters of π Men b		
Orbital period $P_{\rm orb,\,b}$ (days)	$\mathcal{U}[2076.0, 2106.0]$	2091.2 ± 2.0
Time of inferior conjunction $T_{\rm inf,\,b}$ ($\rm BJD_{TDB}-2450000$)	$\mathcal{U}[6528.0, 6568.0]$	6548.2 ± 2.7
$\sqrt{e_{\rm b}} \sin \omega_{\star,\,\rm b}$	$\mathcal{U}[-1, 1]$	-0.3919 ± 0.0076
$\sqrt{e_{\rm b}} \cos \omega_{\star,\,\rm b}$	$\mathcal{U}[-1, 1]$	0.6970 ± 0.0052
Radial velocity semi-amplitude variation $K_{\rm b}$ (m s^{-1})	$\mathcal{U}[0, 500]$	195.8 ± 1.4
Model parameters of π Men c		
Orbital period $P_{\rm orb,\,c}$ (days)	$\mathcal{U}[6.24, 6.29]$	6.26834 ± 0.00024
Transit epoch $T_{0,\,\rm c}$ ($\rm BJD_{TDB}-2450000$)	$\mathcal{U}[8325.47, 8325.52]$	8325.503055 ± 0.00077
Scaled semi-major axis $a_{\rm c}/R_\star$	$\mathcal{N}[13.11, 0.17]$	13.10 ± 0.18
Planet-to-star radius ratio $R_{\rm c}/R_\star$	$\mathcal{U}[0, 0.1]$	0.01721 ± 0.00024
Impact parameter $b_{\rm c}$	$\mathcal{U}[0, 1]$	0.614 ± 0.0180
$\sqrt{e_{\rm c}} \sin \omega_{\star,\,\rm c}$	$\mathcal{F}[0]$	0
$\sqrt{e_{\rm c}} \cos \omega_{\star,\,\rm c}$	$\mathcal{F}[0]$	0
Radial velocity semi-amplitude variation $K_{\rm c}$ (m s^{-1})	$\mathcal{U}[0, 10]$	1.55 ± 0.27
Additional model parameters		
Parameterized limb-darkening coefficient q_1	$\mathcal{N}[0.36, 0.1]$	0.33 ± 0.10
Parameterized limb-darkening coefficient q_2	$\mathcal{N}[0.25, 0.1]$	0.23 ± 0.10
Systemic velocity $\gamma_{\rm AAT}$ (km s^{-1})	$\mathcal{U}[-0.20, 0.20]$	0.0021 ± 0.0011
Systemic velocity $\gamma_{\rm HS1}$ (km s^{-1})	$\mathcal{U}[10.53, 10.88]$	10.70916 ± 0.00039
Systemic velocity $\gamma_{\rm HS2}$ (km s^{-1})	$\mathcal{U}[10.55, 10.90]$	10.73156 ± 0.00071
RV jitter term $\sigma_{\rm AAT}$ (m s^{-1})	$\mathcal{U}[0, 100]$	$4.26^{+1.10}_{-0.96}$
RV jitter term $\sigma_{\rm HS1}$ (m s^{-1})	$\mathcal{U}[0, 100]$	$2.35^{+0.19}_{-0.17}$
RV jitter term $\sigma_{\rm HS2}$ (m s^{-1})	$\mathcal{U}[0, 100]$	$1.69^{+0.39}_{-0.29}$
Derived parameters of π Men b		
Planet minimum mass $M_{\rm b} \sin i_{\rm b}$ ($M_{\rm Jup}$)	···	9.66 ± 0.20
Semi-major axis of the planetary orbit $a_{\rm b}$ (AU)	···	3.22 ± 0.03
Orbit eccentricity $e_{\rm b}$	···	0.6394 ± 0.0025
Argument of periastron of stellar orbit $\omega_{\star,\,\rm b}$ (deg)	···	330.65 ± 0.65
Time of periastron passage $T_{\rm per,\,b}$ ($\rm BJD_{TDB}-2450000$)	···	6306.1 ± 4.6
Derived parameters of π Men c		
Planet mass $M_{\rm c}$ ($M_\oplus$)	···	4.52 ± 0.81
Planet radius $R_{\rm c}$ ($R_\oplus$)	···	2.06 ± 0.03
Planet mean density $\rho_{\rm c}$ (g cm^{-3})	···	2.82 ± 0.53
Semi-major axis of the planetary orbit $a_{\rm c}$ (AU)	···	0.06702 ± 0.00109
Orbit eccentricity $e_{\rm c}$	···	0 (fixed)
Orbit inclination $i_{\rm c}$ (deg)	···	87.31 ± 0.11
Equilibrium temperature[d] $T_{\rm eq,\,c}$ (K)	···	1147 ± 12
Transit duration $\tau_{14,\,\rm c}$ (h)	···	$2.969^{+0.030}_{-0.032}$

Notes. [a]$\mathcal{U}[a, b]$ refers to uniform priors between a and b, and $\mathcal{F}[a]$ to a fixed a value. [b]From spectroscopy and isochrones. [c]From spectroscopy. [d]Assuming zero albedo and uniform redistribution of heat.